5-2019

Reconstruction of Attenuated Hybrid Rocket Motor Chamber Pressure Signals Using Maximum Likelihood Estimation and Optimal Deconvolution

Evan M. Zelesnik
Utah State University

RECONSTRUCTION OF ATTENUATED HYBRID ROCKET MOTOR CHAMBER PRESSURE SIGNALS USING MAXIMUM LIKELIHOOD ESTIMATION AND OPTIMAL DECONVOLUTION

by

Evan M. Zelesnik

A thesis submitted in partial fulfillment
of the requirements for the degree

of

MASTER OF SCIENCE

in

Aerospace Engineering

Approved:

_____	_____
Stephen Whitmore, Ph.D.	David Geller, Ph.D.
Major Professor	Committee Member

_____
Geordie Richards, Ph.D.
Committee Member

UTAH STATE UNIVERSITY
Logan, Utah

2019

ABSTRACT

Reconstruction of Attenuated Hybrid Rocket Motor Chamber Pressure Signals Using Maximum Likelihood Estimation and Optimal Deconvolution

by

Evan M. Zelesnik, Master of Science

Utah State University, 2019

Major Professor: Dr. Stephen A. Whitmore
Department: Mechanical and Aerospace Engineering

Chamber pressure, as it develops during rocket combustion, strongly correlates with many of the internal motor ballistics, including combustion stability, fuel regression rate, and mass flow. Chamber pressure is also an essential measurement for calculating achieved thrust coefficient and characteristic velocity. Due to the combustion environment hostility, sensing chamber pressure with high-fidelity presents a difficult measurement problem, especially for solid and hybrid rocket systems where combustion by-products contain high amounts of carbon and other sooty materials. These contaminants tend to deposit within the pneumatic tubing used to transmit pressure oscillations from the thrust chamber to the sensing transducer. Partially clogged transmission tubes exhibit significant response latency and damp high frequency pressure oscillations that may be of interest to the testers. A maximum-likelihood method for fitting a second order model to chamber pressure response is presented. The resulting model was used to reconstruct a high-fidelity motor response via optimal deconvolution. The method was applied to small hybrid-thruster results from three separate testing

campaigns. Key performance parameters such as thrust coefficient, characteristic velocity, and specific impulse were re-calculated using the reconstructed data. Results were compared to the unreconstructed data, and are shown to exhibit consistently better agreement with theoretical predictions.

(46 pages)

PUBLIC ABSTRACT

Reconstruction of Attenuated Hybrid Rocket Motor Chamber Pressure Signals Using Maximum Likelihood Estimation and Optimal Deconvolution

Evan M. Zelesnik

Chamber pressure is a key parameter of rocket motor combustion, and it is used to calculate important performance benchmarks such as achieved thrust coefficient and characteristic velocity. Due to the combustion environment hostility, sensing chamber pressure with high-fidelity presents a difficult measurement problem, especially for solid and hybrid rocket systems where combustion by-products contain high amounts of carbon and other sooty materials. These contaminants tend to deposit in the pressure lines and sensors. Partially clogged transmission tubes exhibit significant response latency and damp high frequency pressure oscillations that may be of interest to the testers. A maximum-likelihood method for fitting a second order model to chamber pressure response is presented. The resulting model was used to reconstruct a high-fidelity motor response via optimal deconvolution. The method was applied to small hybrid-thruster results from three separate testing campaigns. Key performance parameters such as thrust coefficient, characteristic velocity, and specific impulse were re-calculated using the reconstructed data. Results were compared to the unreconstructed data, and are shown to exhibit consistently better agreement with theoretical predictions.

ACKNOWLEDGMENTS

First and foremost I would like to thank Dr. Stephen Whitmore for his continued guidance and support for all things rockets. Without him this work would surely not have been possible. Additional thanks to my committee members, Dr. David Geller and Dr. Geordie Richards.

I am deeply grateful to my family and friends who supported and encouraged me throughout this whole endeavor. Thank you to Amanda Buening, in particular, who always helps keep things in perspective. Special thanks to my dad for instilling in me an appreciation for and interest in rockets in the first place.

Finally, I would like to thank my dog, Sadie, for her endless encouragement to take much-needed fetch breaks.

Evan M. Zelesnik

CONTENTS

Page

LIST OF TABLES

LIST OF FIGURES

ACRONYMS

ABS	acrylonitrile butadiene styrene
CEA	Chemical Equilibrium with Applications
CF	thrust coefficient
ER	expansion ratio
FDM	fused deposition modeling
GOX	gaseous oxygen
MSFC	Marshall Space Flight Center
N20	nitrous oxide
NASA	National Aeronautics and Space Administration
PRDL	Propulsion Research and Development Laboratory
USU	Utah State University

NOMENCLATURE

A^*	nozzle throat area, m^2
C_F	thrust coefficient
C^*	characteristic velocity, *m/s*
F	thrust, *N*
I_{sp}	specific impulse, *s*
L^*	characteristic length, *m*
$\dot{m}$	massflow rate, *kg/s*
n	number of tests
P_0	chamber pressure, *psia*
O/F	oxidizer to fuel ratio
R_g	universal gas constant, *J/kg-K*
S_x	sample standard deviation
t	burn time, *s*
T_0	combustion chamber temperature, ℃
V_c	combustion chamber volume, m^3
$\bar{x}$	sample mean
γ	ratio of specific heats
ς	damping ratio
η^*	combustion efficiency
μ	true mean
ρ	fuel density, kg/m^3
τ	time constant, *s*
$\tau_{c\%}$	student-t multiplier for c% confidence level and n-1 degrees of freedom
ω_n	natural frequency, *Hz*

CHAPTER 1

INTRODUCTION

Chamber pressure (P_0), as it develops during rocket combustion, is a key parameter that strongly correlates with many of the internal chamber ballistics, combustion stability, fuel regression rate, mass flow, and thrust. For low thrust levels, measurements of chamber pressure often provide higher fidelity information with regard to thrust onset and decay and total delivered impulse, which are typically quite noisy when sensed using direct load measurements. Finally, chamber pressure is an essential measurement for calculating achieved thrust coefficient (C_F), characteristic velocity (C*), and combustion efficiency (η*). Chamber pressure is of critical importance for solid and hybrid rockets, where the fuel regression rate is directly tied to chamber pressure or the rate of oxidizer mass flux.

The chamber pressure of a typical rocket-motor burn exhibits both transient and steady-state phases. During the transient ignition phase, the evolution of chamber pressure is driven by the imbalance between incoming mass flow and the nozzle choke condition. The rise in chamber pressure during ignition is typically quite fast, and the precise rate of growth is highly dependent on the type of system – mono-prop, liquid bi-prop, solid, or hybrid, and the choice of propellants. Another important transient phase occurs near the end of the burn, where the fuel grain (or in the case of a hybrid motor, the oxidizer) is mostly consumed. Variations of chamber pressure during the steady-state burn period result from the receding fuel grain surface, fuel regression rate variations, nozzle throat erosion, and combustion instability.

Due to the hostility of the combustion chamber flow environment, obtaining

accurate, high-fidelity, motor chamber-pressure measurements can be a difficult sensing problem. A typical installation taps the motor case, injector head, or post-combustion chamber at the desired location(s) using a small pressure port, and then transmits the pressure from the port to a pressure transducer using a significant length of pneumatic tubing. This installation allows the transducer to be mounted in a low temperature environment. Typically, the pneumatic transmission tube is bent at 90 degrees or greater in order to prevent the direct impingement of high-intensity plume radiation directly upon the transducer diaphragm.

Within this pneumatic installation, acoustical distortion due to friction, acoustical resonance and latency, and wave reflections will compromise the fidelity of the sensed pressure measurement. If the resulting frequency response is too low, then important events such as ignition transients or combustion instabilities may be attenuated or missed altogether. Often the internal geometry of the tube/sensor configuration is not well known, and flow constrictions, tube fittings, embedded filters, and clogged or dirty inlet ports can additionally complicate the flow path dynamics.

During testing of 3-D printed hybrid rocket systems small spacecraft, such a low-fidelity pressure response scenario was regularly encountered.[1] The hybrid thruster for this testing campaign used gaseous oxygen (GOX) and 3-D printed acrylonitrile butadiene styrene (ABS) as propellants. At the small scales experienced by these thrusters, both convective heat-transfer within the boundary layer, and radiation heating from the flame zone fuel wall significantly influenced the fuel regression rate. At the low oxidizer massflow rates required for these thrust levels, radiation heating tends to be of the same initial magnitude as convective heating. As the fuel grain burns and the port

opens up, convective heating tends to drop off, and radiation heating begins to dominate. The result is that the oxidizer-to-fuel (O/F) ratio of the motor tends to shift from lean to rich, and for the majority of motors tested, the plume tends to become progressively sootier. The observed "anomalous" fuel-rich (negative) O/F shift is in direct contrast to the behavior observed for larger scale hybrid motors, which nearly always shift from rich to lean.[2]

A negative side effect of the fuel-rich shift is that the pneumatic tubing of the chamber pressure sensor gradually become partially-clogged with burned hydrocarbons, significantly reducing the response fidelity of the measurement system. Cleaning the hydrocarbons from the tubing is extremely difficult, and often requires that the sensors be disassembled and the transmission tubing must be completely replaced. For the testing campaigns of Refs. [1] and [2], the reduced frequency response was not discovered until the testing campaign was concluded.

A key objective of the studies performed by Refs. [1] and [16] was to characterize the repeatability and response fidelity of these small spacecraft thrusters when operated in pulse mode with a string of successive small-duration pulses being performed. The resulting pneumatic attenuation significantly compromised the test results. Reassembling the systems and repeating the tests, continually cleaning the chamber pressure assembly between tests, was both economically and practically infeasible. Instead, the optimal deconvolution method developed by Whitmore and Wilson[3] were adapted to compensate for the attenuation caused by the dirty pressure transmission paths.

In the methods of Ref. [3], the tubing response model was analytically calculated using the methods of Berg and Tijdeman[4] based upon known installation geometries for

tubing lengths and diameters, and the entrapped sensor volume. The resulting analytically-derived transfer function was subsequently submitted to a deconvolution algorithm, derived from Wiener theory, that allows accurate high-fidelity input pressure trajectories to be reconstructed. When properly tuned, the derived method amplifies the attenuated pressure signals, while selectively rejecting the contaminating measurement noise. For well-defined measurement geometries, the method of Ref. [3] offers a useful tool for obtaining unsteady pressure measurements, and represents an alternative to conventional in situ mounting methods for measuring high-frequency fluctuating pressures in difficult or hostile environments.

Because of the unknown effects of the combustion product contamination within the pressure transmission lines, fittings, and other components, a purely analytical method could not be used for this analysis. Instead, the natural response decay of the chamber pressure trace, after the termination of oxidizer flow for each thruster pulse is curve fit with a second-order response model, and this transfer function is used to perform the optimal deconvolution of the highly attenuated pressure signal.

Based on the work of Whitmore and Fox,[5] who demonstrated that a simple linear second-order transfer function can accurately capture the dominant acoustical harmonic in a typical pressure sensing system, and the anticipated high level of attenuation of higher order harmonics, the second-order model was deemed to offer an acceptable level of compromise between simplicity and accuracy. By assuming that the pressure tail off results from a step input, the damping ratio and natural frequency of the response model were identified using well-developed maximum likelihood parameter estimation tools and methods.[6]

This paper will present the development of the estimation methods used to identify the attenuation model parameters, and subsequently apply the derived model to deconvolve the high-fidelity system response from the attenuated measured pressure time histories. Multiple response time histories will be examined and corrected for the effects of pneumatic attenuation. Comparing the original and deconvolved pressure signals, the effects of the deconvolution on the end-to-end thruster system performance will be presented.

CHAPTER 2

SMALL THRUSTER SYSTEM BACKGROUND

The Propulsion Research Laboratory at Utah State University recently developed a promising "green" alternative to current space propulsion systems that are based on environmentally unsustainable hydrazine propellants. The power-efficient USU system can be started and restarted with a high degree of reliability. This alternative system concept derives from the unique electrical breakdown properties of 3-D printed acrylonitrile butadiene styrene (ABS), discovered while investigating the thermodynamic performance of ABS as a hybrid rocket fuel.[7] The layered structure of the printed ABS provides small-radii surface features. When electrodes are embedded into the structure and voltage is applied across the electrodes, these features concentrate charge at many discrete points on the material surface and allow a strong electrical arc to occur at moderate voltage levels. The electric field generated by the arc produces joule-level heating and results in fuel pyrolysis along the conduction path. When a combustible gas is introduced, mixture with the pyrolyzed fuel rapidly leads to a self-sustaining combustion along the entire fuel port surface.[8,9]

2.1 Small Thruster Test Campaign Summary

After proof of concept tests with the ignitor and lab-scale integration tests were completed, an effort was made to scale down the thruster to a flight-weight system that would be generally applicable for SmallSat operations. An analytical hybrid flow model[10] was used to design a flight-weight unit with a desired 25-N thrust level. Both ambient pressure and vacuum tests were performed. Whitmore and Mathias[11] give a complete description of the test stand and the instrumentation system used to collect the ambient

measurements.

The flight-weight thruster system was vacuum tested during the summer of 2016 in the NASA Marshall Space Flight Center's (MSFC) Propulsion Research and Development Laboratory (PRDL). Test objectives included 1) demonstration of reliable multiple restart capability under near vacuum conditions, 2) characterization of the vacuum specific impulse with a high expansion ratio (ER) nozzle, 3) characterization of the system startup time under vacuum conditions, 4) identify any possible corona discharge effects due to the high-ignition voltage at low operating pressure levels, 5) measure the plume contamination levels. The motor and test system described in the previous section were modified to fit into the vacuum chamber. Whitmore and Bulcher (2017, Ref [1]) present a detailed description of the vacuum testing campaign, including the measurement systems and preliminary test results. Whitmore and Brewer[12] present the details of the plume contamination measurements.

2.2 Suborbital Space Flight Test

This arc-ignition concept has been developed into a power-efficient system that can be started and restarted with a high degree of reliability. Multiple successive ignitions have been successfully demonstrated with both nitrous oxide (N20)[13] and gaseous oxygen (GOX) as oxidizers.[2] Multiple prototype ground-test units with thrust levels varying from 4.5 N to 900 N have been developed and tested.[14] Recently, on March 25th, 2018 a flight experiment containing a medium-weight prototype of this thruster system was launched aboard a two-stage Terrier-Improved Malemute sounding rocket from Wallops Flight Facility (WFF). The launch achieved apogee of 172 km, allowing more than 6 minutes in a true space environment above the Von- Karman line. During the mission the USU

thruster was successfully fired 5 times in a hard vacuum environment. The payload section was successfully recovered by WFF flight support. Low-resolution telemetry data was successfully downlinked and delivered to USU for analysis. Whitmore and Bulcher (2018) report the details of this flight test experiment.[1]

2.3 Thrust Chamber Layout

Figure 1 presents the details of the thrust chamber assembly. Figure 1(a) presents a 2-D schematic of the 38 mm thrust chamber. Figure 1(b) compares the 1-G (Short), and 2-G (long) 38-mm thrust chamber assemblies. Depicted are the major components; i) graphite nozzle, ii) nozzle retention cap, iii) motor case, iv) 3D printed fuel grain with embedded electrodes, v) insulating phenolic liner, vi) chamber pressure fitting, and vii) single-port injector cap. The 38-mm diameter thrust chamber is constructed from 6061-T6 high-temperature aluminum, and was procured commercially from Cesaroni Inc.[*] Two motor case lengths were available from Cesaroni; a "1-G" configuration that accepts a fuel grain of length up to 6.85 cm, and a "2-G" configuration that accepts a longer fuel grain with length of up to 12.69 cm. For ambient test conditions the nozzle expansion ratio was 2.06:1, and was approximately optimal for the test altitude in Logan Utah. The vacuum test nozzle expansion ratio was 9:5:1, and was approximately optimal for the expected vacuum chamber pressures that could be achieved with the motor firing. Table 1 summarizes the 25 Newton thruster geometry and other specifications.

[*] Anon., "Cesaroni Pro-X, A Better Way to Fly, Pro 38® hardware," http://pro38.com/products/pro38/pro38.php, [Retrieved 5 January, 2019].

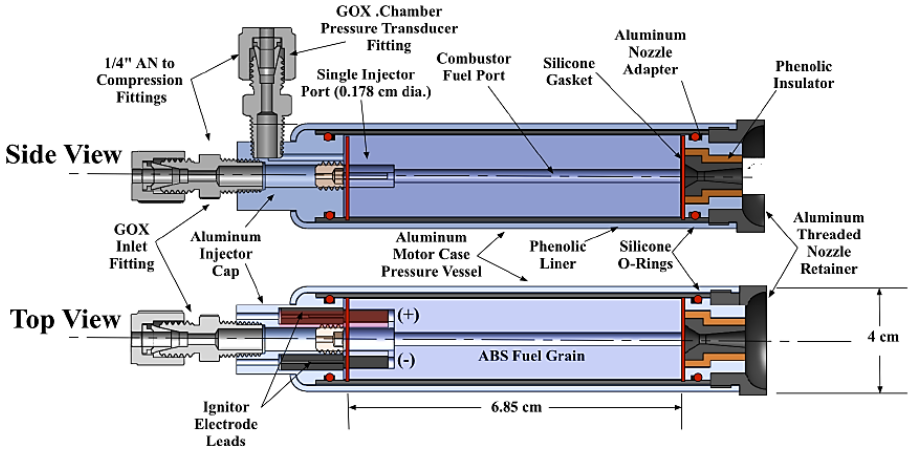

a) 2-D Schematic

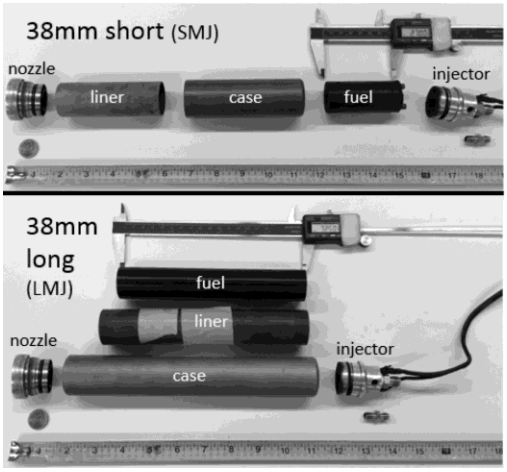

b) Thrust Chamber Assemblies

Fig. 1 Test Article Thruster Assembly

Table 1 Motor Geometry and Parameter Specifications

Parameter	Injector		Single Port, 0.127 cm (0.05 in.) Diameter	
Fuel Grain	Diameter: 3.168 cm (1.247 in.)	Length: 6.850 cm (1-G) 12.69 (2-G)	Initial Weight: High Density: 50.0 g	Initial Port Diameter: 0.625 cm (0.246 in.)
Motor Case	Diameter: 3.8 cm (0.150 in.)	Length: 13.8 cm (5.43 in.)	Wall Thickness: 1.5 mm (0.059 in)	
Low Expansion Ratio Nozzle	Initial Throat Diameter: 0.401 cm (0.158 in.)	Exit Diameter: 0.576 cm (0.227 in.)	Ambient Tests Initial Expansion Ratio: 2.06:1	Nozzle Exit Angle: 5.0 deg.
High Expansion Ratio Nozzle	Initial Throat Diameter: 0.422 cm (0.166 in.)	Exit Diameter: 1.300 cm (0.512 in.)	Vacuum Tests Initial Expansion Ratio: 9.5:1	Nozzle Exit Angle: 20.0 deg.

2.4 Fuel Grain Design

The fuel grains for this thruster system are specially designed and additively manufactured. Figure 2 shows the pre-combustion chamber design that features two impingement shelves intended to trap and mix the injected oxidizer with the pyrolyzed fuel. All test fuel grains were fabricated using a Stratasys Dimension 1200-ES® fused deposition model (FDM) printer.[†] Using available ABS plus-340® feed-stock[‡], the approximate fuel print density is 0.975 g/cm^3.

Fig. 2 FDM Printed Fuel Grain with ESC-Terminated Electrodes

Motor ignition relies on the patented arc-ignition system developed at Utah State University by Refs. [8] and [13]. The fuel grains used for this test series are based on a standardized design developed at the USU Propulsion Research Laboratory. Two electrodes, insulated by industry standard ESC-connectors,[§] are embedded into the top face of the fuel grain. Wires are routed from the electrodes to small gaps located on the

[†] Anon., "Dimension 1200ES, Large, Durable Parts, http://www.stratasys.com/3d-printers/design-series/dimension-1200es, [Retrieved 25 Jul. 2016].
[‡] Anon., "ABSplus Spec Sheet," http://usglobalimages.stratasys.com/Main/Secure/Material%20Specs%20MS/Fortus-Material-Specs/Fortus-MS- ABSplus-01-13-web.pdf, [Retrieved 25 Jul. 2016].
[§] Anon., "Motor to ESC Connectors," https://www.motionrc.com/collections/motor-to-esc-connectors, [Retrieved 6 June 2017].

impingement shelves. The wires are insulated by printed circular sots that insert into the electrode wire gaps. The conducting paths terminate facing each other, flush with the combustion port surface, and exposed to the interior of the combustion chamber.

2.5 Effect of Fuel Grain Length on Motor Burn Properties

The choice of motor length significantly influenced the oxidizer-to-fuel ratio (O/F) for the system, with the shorter motor producing O/F ratios varying from 1.5 to slightly greater than 3. The longer motor resulted in significantly lower O/F ratios with values varying from approximately 0.4 to slightly less than 1.0. This low O/F had several effects, notably lowering combustion flame temperature, and producing a large percentage of sooty particulates in the rocket plume.

Figure 3 shows a prototype 1-G flight weight unit with an additively-manufactured ABS fuel grain during static hot-firing with gaseous oxygen (GOX) as the oxidizer. The plume shown is the product of an approximate 2.1:1 expansion ratio nozzle with an operating chamber pressure of 125 psia. Notice the bright, clear, soot free flame that is produced.

Fig. 3 Hot-fire Test of Prototype 25-N Thruster Unit with 1-G Thrust Chamber

However, once the motor case was swapped for the 2-G version and the accompanying longer fuel grain, the burn properties changed significantly. The burn time history "slideshow" of Figure 4 shows this tendency for the motor to burn richer with time. From top to bottom these images depict, i) GOX ignition, ii) Steady state flow with shock diamonds formed, iii) End of steady state flow, plume noticeably fuel rich, and iv) Motor cutoff. The total depicted burn duration is approximately 4 seconds.

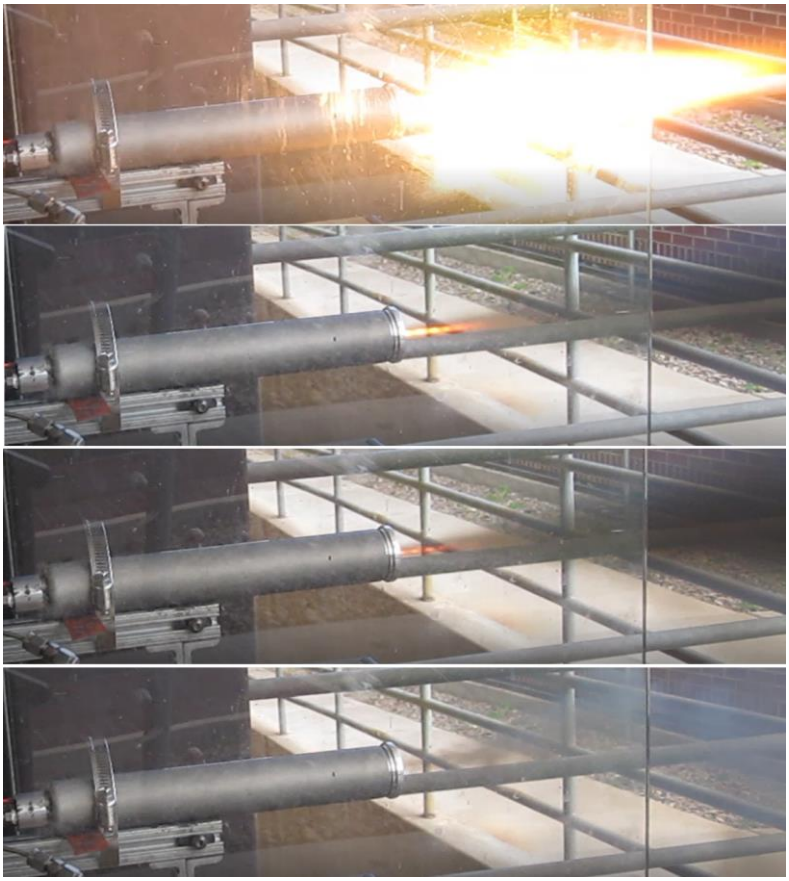

Fig. 4 2-G Longer-Grain Thruster Time Lapse Burn Images

Even with the short-grain configuration, all burns exhibited a negative O/F shift as a function of burn lifetime, and even the 1-G configurations became fuel-rich and

sooty after 10-15 seconds of total burn lifetime. As described previously, this negative O/F shift is mostly attributable to the effect of radiation heating in very small hybrid rockets. Whitmore and Merkley (2016) present a thermodynamic model describing the negative O/F shift, and detailing the reasons for this "anomalous" behavior.[15]

2.6 Effect of O/F Ratio on Motor Performance and Burn Temperature

Assuming GOX and ABS as propellants, Figure 5 compares the operating O/F ranges of the test motor using the short and long fuel grains against theoretical calculations[16] of the chamber combustion temperature T_0, and 100% efficient characteristic velocity C*. For these propellants the stoichiometric O/F ratio is approximately 2.0, with a best performance occurring at an O/F of approximately 1.5.

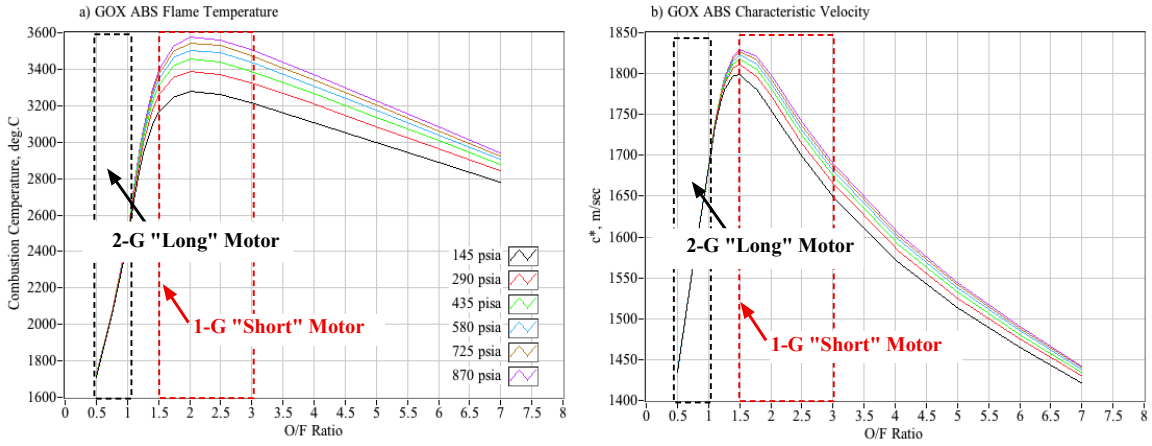

Fig. 5 Comparing Flame Temp. and C* of Long (2-G) & Short (1-G) Fuel Grains

Swapping from the short (1-G) to the long (2-G) motor lowers the performance by slightly greater than 10%. More significantly, this swap also lowers the flame temperature by more than 1200 ^{o}C. This reduction in flame temperature would significantly increase the operating lifetime of the nozzle throat, especially under vacuum

conditions where passive convection is not available to cool the nozzle.

2.7 Effect of Plume Contamination on Measured Chamber Pressure Response

As described earlier, this fuel-rich operation of the thrust chambers eventually introduces contaminants into the pneumatic arrangement that is used to deliver the chamber pressure to the sensing pressure transducer. Figure 6 shows a typical multiple-pulse burn of the 25-N thruster system, collected by Ref. [1] during vacuum chamber tests performed in the Chemical Synthesis Laboratory at the NASA Marshall Space Flight Center (MSFC). Plotted are (a) thrust, (b) chamber pressure, (c) oxidizer massflow, (d) vacuum pressure, (f) ignition current, and (f) ignition voltage. At the plotted scale, the burns appear to be quite crisp with a rapid rise and drop after termination of the oxidizer flow.

However, when the burns are scaled up in time, the behaviors appear quite different. Figure 7 shows a detailed close up of the 8 pulses overlaid so that the start times originate at time zero. Plotted are (a) the oxidizer massflow and (b) chamber pressure. For these burns the ignition current initiates 500 ms ahead of the main valve opening. Note that the GOX massflow for the individual pulses are essentially identical, but that the chamber pressure curves all take on slightly different shapes. Also note that the tail off of each pulse is significantly longer than the oxidizer flow tail off – 500 ms as opposed to 80 ms.

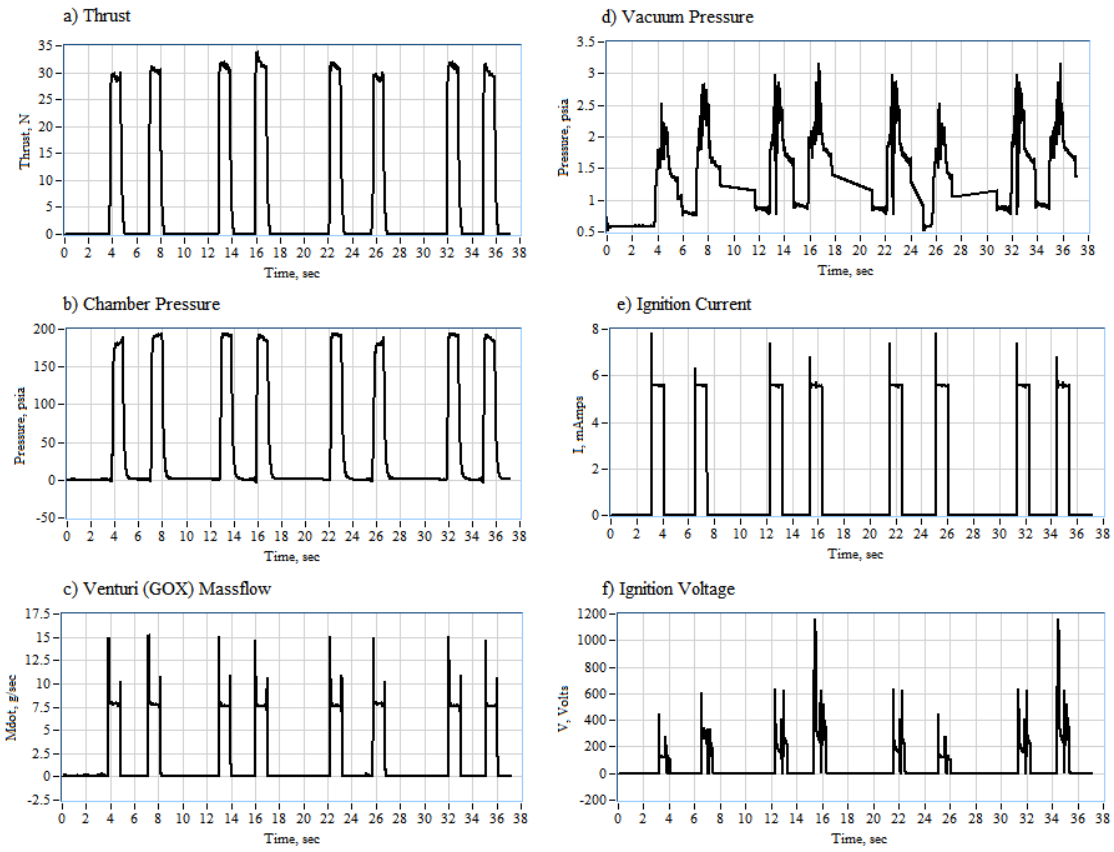

Fig. 6 Data from 25 Newton Thruster System in MSFC Vacuum Chamber

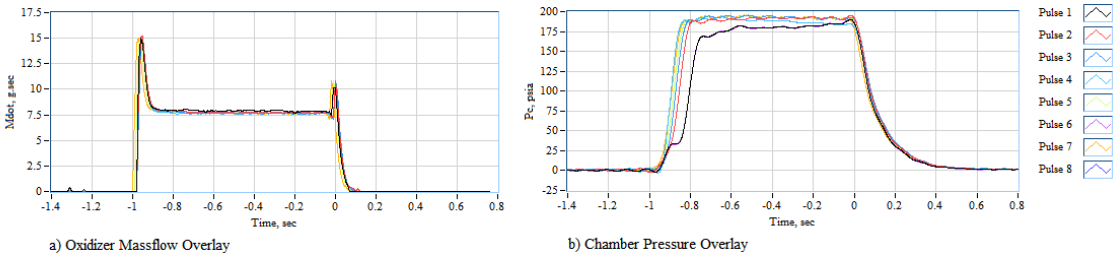

Fig. 7 Overlay of the 8 Pulse Burns from Figure 6

2.8 Chamber Pressure Tail Off Ballistic Analysis

Following termination of the oxidizer flow, the observed chamber pressure tail offs of Figure 7, nearly 1/2 second each, are significantly larger than would be expected based on the internal thrust chamber ballistics alone. It can be shown that for choked

nozzle and no external mass flow forcing, the chamber pressure time decay is approximately first order[17] with

$$P_0(t)_{tailoff} = P_{0_{ss}} \cdot e^{-\frac{\left(t - t_{burnout}\right)}{\tau_{combustor}}} \tag{1}$$

where

$$\tau_{combustor} = \frac{L^*}{\sqrt{\gamma \cdot R_g \cdot T_0 \cdot \left(\frac{2}{\gamma+1}\right)^{\frac{\gamma+1}{\gamma-1}}}} \tag{2}$$

The parameters γ, R_g, and T_0 are the ratio of specific heats, gas constant, and flame temperature of the combustion products at the time of motor burnout, and L* is the combustion chamber characteristic length, given by

$$L^* = \frac{V_c}{A^*} \tag{3}$$

In Eq. (3) V_c is the internal combustion chamber volume, and A* is the nozzle throat area. For GOX/ABS Propellants, Figure 8 plots the ratio $\tau_{combustor}/L^*$ from Eq. (2) as a function of O/F ratio and chamber pressure, assuming 100% combustion efficiency. (Ref. [17])

The characteristic length of the fuel port grows with time as the fuel port opens up and can be approximated by

$$L^* = \frac{1}{A^*}\left(\frac{\pi \cdot D_{initial}^2 \cdot L_{port}}{4} + \frac{M_{burn}}{\rho_{fuel}}\right) = \frac{1}{A^*}\left(\frac{\pi \cdot D_{initial}^2 \cdot L_{port}}{4} + \frac{1}{O/F}\frac{\dot{m}_{ox} \cdot t_{burn}}{\rho_{fuel}}\right) \tag{4}$$

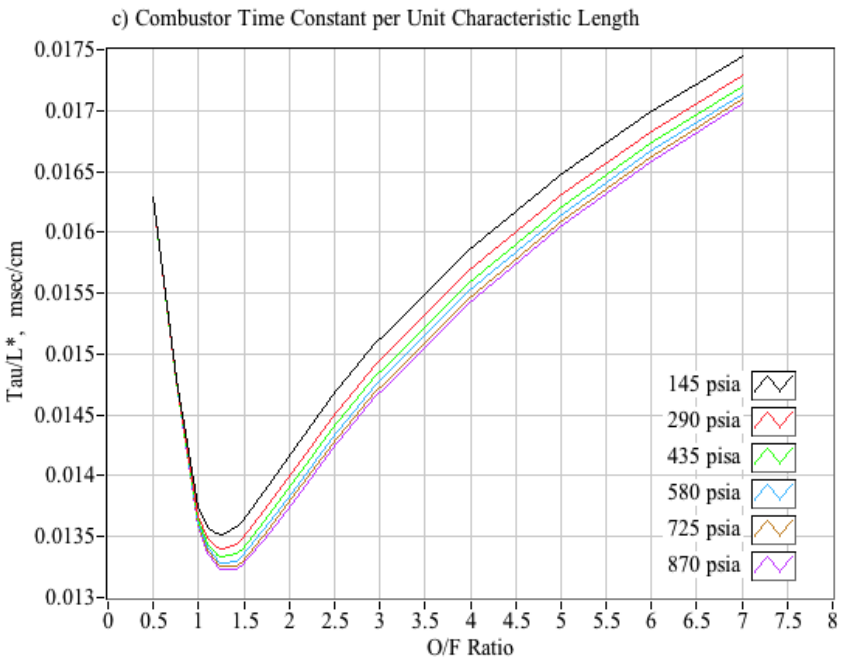

Fig. 8 Ballistic Time Lag Per Unit Characteristic Length

In Eq. (4) $D_{initial}$ is the initial fuel port diameter (0.625 cm) and L_{port} is the fuel port length (6.85 cm). It is observed from Figs. 6 and 7 that the oxidizer massflow for each burn is a consistent 7.8 grams per second. Based on the 1-G motor configuration, Figure 5 shows a median O/F ratio of approximately 2.25 for this burn series. For 180 psia chamber pressure, and O/F equal to 2.25, Figure 8 shows that the approximate ratio $\tau_{combustor}/L^*$ is 0.143 ms/cm.

Using the above prescribed numerical values, the thrust chamber characteristic length, L*, and time-constant, $\tau_{combustor}$, can be calculated as a function of the thruster burn time, and over the range of operating O/F ratios from 1.5 up to 3.0. Figure 9 plots these results. Note that the maximum chamber ballistics time constant occurs for the 8th burn, and even then it is only 5 ms. This value is roughly 100 times smaller than the approximately 1/2 second latency observed in Figure 7b. Thus, the ballistic response of

the delay combustion chamber is essentially negligible, and the slow response of the chamber pressure time history measurement must be attributable to the latencies and damping of the measurement configuration. The measurement configuration includes the pressure tap at the injector cap, transmission tubing, tube bend, transducer fitting, internal transducer volume, and any entrapped contaminants.

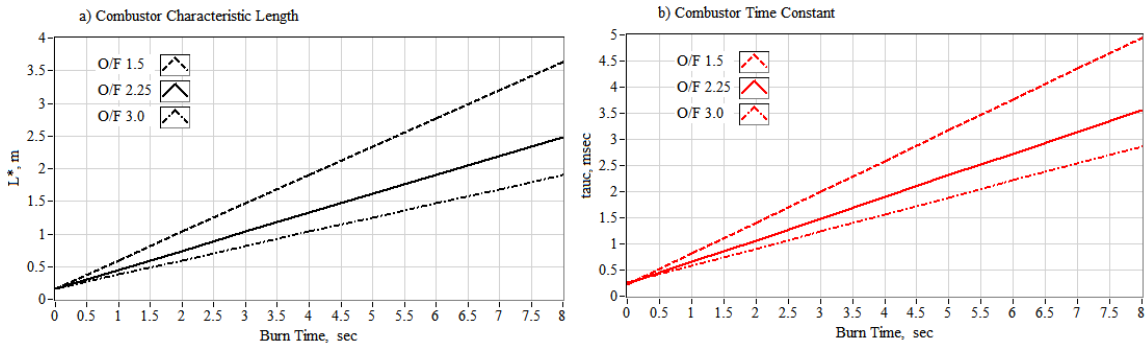

Fig. 9 Combustion Chamber L* and Time Constant as Function of Burn Time

CHAPTER 3

MODELING THE CHAMBER PRESSURE TAIL OFF

Figure 10 presents an idealized schematic of a typical pressure sensing system layout. The configuration is modeled as a straight cylindrical tube with a dimensionless (no length) volume, V, representing the internal volume of the pressure transducer attached to the downstream end. A longitudinal coordinate, x, is defined as positive moving aft from the upstream (port) end of the tube. The symbols L and D represent the tube length and diameter, respectively. The cross sectional area of the tube, Ac, is assumed to be constant. Unsteady surface pressure impulses $P_0(t)$, propagate as longitudinal waves down the tube and are sensed by the pressure transducer as $P_L(t)$.

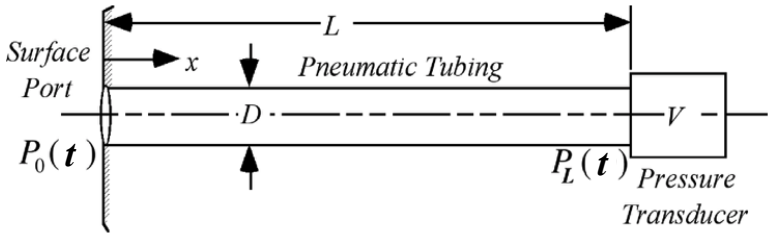

Fig. 10 Schematic of Idealized Pressure Sensor Configuration

As described previously, Ref. [5] has demonstrated that the dominant mode of the full order harmonic model can be approximated by a simple second-order dynamic model of the form

$$\frac{d^2 P_{L(t)}}{dt^2} + 2 \cdot \varsigma \cdot \omega_n \cdot \frac{dP_{L(t)}}{dt} + \omega_n^2 \cdot P_{L(t)} = \omega_n^2 \cdot P_{0(t)} \tag{5}$$

where $P_L(t)$ is the sensed pressure response at the transducer, and $P_0(t)$ is the input to the pneumatic transmission system. For the simple configuration as depicted by Figure 10,

the expressions for damping ratio, natural frequency, and time lag can be written analytically as

$$\omega_n^2 = \frac{\frac{A_c c^2}{LV}}{\frac{L \cdot A_c}{2V}\left[1+\frac{256}{3}\frac{\gamma}{P_0\rho_0}\left(\frac{\mu \cdot L}{D^2}\right)^2\right]+\left[1+\frac{512}{3}\frac{\gamma}{P_0\rho_0}\left(\frac{\mu \cdot L}{D^2}\right)^2\right]}$$

$$\varsigma = \frac{\omega_n}{2}\left(128\frac{\mu L}{\pi D^4 P_0}\right)\left(V+\frac{L \cdot A_c}{2}\right)$$

$$\tau = 128\frac{\mu L}{\pi D^4 P_0}\left(V+\frac{L \cdot A_c}{2}\right) \tag{6}$$

In Eq. (6) the geometric parameters are as previously defined and the parameters c, ρ, and μ are the local sonic velocity, the input fluid density, and the dynamic viscosity. Because the installation geometry being considered here is quite a bit more complex than depicted by Fig. (10), and also allowing for the burned hydrocarbons that contaminate the flow path, the analytical expressions of Eq. (6) tend to significantly under predict the associated damping, attenuation, and response latency.

3.1 Modeling the Pressure Tail Off Curve as a Second-Order Step Response

Instead, the approach to be taken here will model the natural decay of the sensor as the response of a second-order model to a step input, where the input to the pressure sensing system drops from the steady state chamber pressure to the local ambient pressure level. Figure 11 illustrates this concept. The "initial" value is the steady-state chamber pressure just before the oxidizer flow termination. The "step input" is then the difference between the "initial" and "final" values, or the difference between the local ambient pressure level and the final steady state pressure level. The red trace of Fig. 10

represents the best-fit response of the second order model to the negative step input.

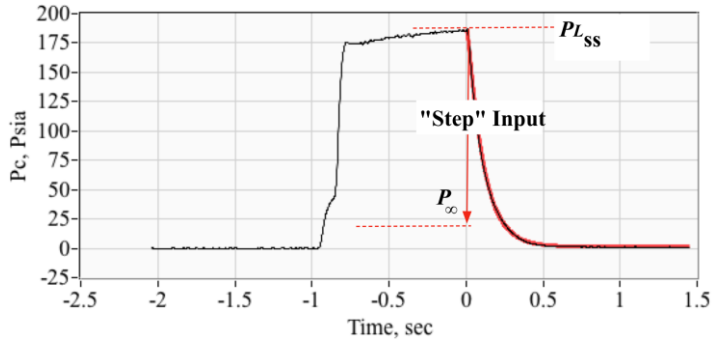

Fig. 11 "Step" Input Modeled as Difference Between Ambient and Final Steady State Pressure Levels

Depending upon the system damping-ratio, there exist three possible analytical solutions for the step response of a linear second-order system. The analytical solutions of Eq. (5) assume the time scale has been shifted so that the step input occurs at t = 0. The parameter $P_{L_{SS}}$ is the final steady state pressure before the termination of the oxidizer flow, and P_∞ is the (final) ambient pressure for the test conditions. The unknown parameters of Eq. (5) are the damping ratio, ζ, and natural frequency, ω_n. The values of the initial ($P_{L_{SS}}$) and final (P_∞) conditions are known from observation of the time history plot. The underdamped, critically-damped, and overdamped solutions to Eq. (5) are provided below in Eq. (7).

$t \geq 0$:

$$1)\ \varsigma < 1: \quad P_{L(t)} = P_\infty + \left(P_{L_{ss}} - P_\infty\right)\left\{e^{-\varsigma\omega_n t}\left[\frac{\varsigma}{\sqrt{1-\varsigma^2}}\sin\left(\sqrt{1-\varsigma^2}\,\omega_n t\right) + \cos\left(\sqrt{1-\varsigma^2}\,\omega_n t\right)\right]\right\}$$

$$2)\ \varsigma = 1: \quad P_{L(t)} = P_\infty + \left(P_{L_{ss}} - P_\infty\right)e^{-\omega_n t}\left(\omega_n t + 1\right)$$

$$3)\ \varsigma > 1: \quad P_{L(t)} = P_\infty + \left(P_{L_{ss}} - P_\infty\right)\left\{e^{-\varsigma\omega_n t}\left[\frac{\varsigma}{\sqrt{\varsigma^2-1}}\sinh\left(\sqrt{\varsigma^2-1}\ \omega_n t\right) + \cosh\left(\sqrt{\varsigma^2-1}\ \omega_n t\right)\right]\right\}$$

$t < 0$: $\quad P_{L(t)} = P_{L_{ss}}$ (7)

3.2 Estimating the Model Parameters

Using the over-damped solution as an example, and non-dimensionalizing the analytical solution model

$$\Pi(t) \equiv \frac{P_L(t) - p_\infty}{P_{L_s} - p_\infty} = \left\{ e^{-\zeta \omega_n t} \left[\frac{\zeta}{\sqrt{\zeta^2 - 1}} \sinh\left(\sqrt{\zeta^2 - 1}\ \omega_n t \right) + \cosh\left(\sqrt{\zeta^2 - 1}\ \omega_n t \right) \right] \right\} \tag{8}$$

Using the response time history, $P_L(t)$, the output error approach[6] is used to estimate the parameters that result in the best quadratic fit, i.e. minimize the quadratic cost function

$$J = \frac{1}{2} \sum_{i-0}^{N} \left[\Pi(t_i) - \widehat{\Pi}(t_i) \right]^2 =$$

$$\frac{1}{2} \sum_{i-0}^{N} \left[\Pi(t_i) - \left\{ e^{-\widehat{\zeta}\widehat{\omega}_n t} \left[\frac{\widehat{\zeta}}{\sqrt{\widehat{\zeta}^2 - 1}} \sinh\left(\sqrt{\widehat{\zeta}^2 - 1}\ \widehat{\omega}_n t \right) + \cosh\left(\sqrt{\widehat{\zeta}^2 - 1}\ \widehat{\omega}_n t \right) \right] \right\} \right]^2 \tag{9}$$

In Eq. (9) the (^) designates a numerical estimate of the parameters (ζ, ω_n). The necessary condition for minimizing J is

$$\nabla_\xi J = 0$$

Expanding the cost function in a power series and evaluating the gradient facilitates the solution.

$$\nabla_\xi \left(J_{\xi_j} + \nabla_\xi J_j \ \left(\xi - \xi_j \right) + \frac{1}{2} \left(\xi - \xi_j \right)^T \nabla^2{}_\xi J_j \cdot \ \left(\xi - \xi_j \right) + \ldots \right) = 0 \tag{10}$$

Truncating after second order and letting the true parameter solution now be approximated by an estimate, $\xi = \xi_{j+1}$, gives

$$\nabla_\xi J_j + \nabla^2{}_\xi J_j \cdot \ \left(\xi_{j+1} - \xi_j \right) = 0 \tag{11}$$

Solving for ξ_{j+1} gives

$$\xi_{j+1} = \xi_j - \left(\nabla^2{}_{\xi} J_j\right)^{-1} \nabla_{\xi} J_j \tag{12}$$

Equation 12 is the classical Newton-Raphson algorithm.[18] The gradients of Eq. (12) are evaluated as

$$\begin{aligned}
\nabla_{\xi} J_j &= \nabla_{\xi}\left(\frac{1}{2}\sum_{i=0}^{N}\left[\Pi(t_i) - \widehat{\Pi}(t_i)_{\hat{\xi}_j}\right]^2\right) = -\sum_{i=0}^{N}\left[\Pi(t_i) - \widehat{\Pi}(t_i)_{\hat{\xi}_j}\right]\nabla_{\xi}\widehat{\Pi}(t_i)_{\xi_i} \\
\nabla^2{}_{\xi} J_j &= \nabla_{\xi}\left(-\sum_{i=0}^{N}\left[\Pi(t_i) - \widehat{\Pi}(t_i)_{\hat{\xi}_j}\right]\nabla_{\xi}\widehat{\Pi}(t_i)_{\xi_i}\right) = \sum_{i=0}^{n}\nabla_{\xi}\widehat{\Pi}(t_i)_{\xi_i}\nabla^T{}_{\xi}\widehat{\Pi}(t_i)_{\xi_i} - \sum_{i=0}^{N}\left[\Pi(t_i) - \widehat{\Pi}(t_i)_{\hat{\xi}_j}\right]\nabla^2{}_{\xi}\widehat{\Pi}(t_i)_{\xi_i}
\end{aligned} \tag{13}$$

The second gradient of the pressure model presents a potential numerical instability problem, so the second gradient of the cost function is evaluated using the Gauss-Newton approximation

$$\nabla^2{}_{\xi} J_j \approx \sum_{i=0}^{n}\nabla_{\xi}\widehat{\Pi}(t_i)_{\xi_i}\nabla^T{}_{\xi}\widehat{\Pi}(t_i)_{\xi_i} \tag{14}$$

The collected minimization algorithm is

$$\xi_{j+1} = \xi_j + \left(\sum_{i=0}^{n}\nabla_{\xi}\widehat{\Pi}(t_i)_{\xi_i}\nabla^T{}_{\xi}\widehat{\Pi}(t_i)_{\xi_i}\right)^{-1}\left(\sum_{i=0}^{N}\left[\Pi(t_i) - \widehat{\Pi}(t_i)_{\hat{\xi}_j}\right]\nabla_{\xi}\widehat{\Pi}(t_i)_{\xi_i}\right) \tag{15}$$

Equation 15 is numerically efficient in that it only requires evaluation of the first Jacobian of the second order pressure model. Equation 15 is more clearly written as a scalar breakout with the model derivatives shown explicitly

$$\xi_{j+1} = \xi_j + \left(\sum_{i=0}^{n}\begin{bmatrix}\dfrac{\partial\widehat{\Pi}}{\partial\varsigma} \\ \dfrac{\partial\widehat{\Pi}}{\partial\omega_n}\end{bmatrix}_{\xi_i}\begin{bmatrix}\dfrac{\partial\widehat{\Pi}}{\partial\varsigma} & \dfrac{\partial\widehat{\Pi}}{\partial\omega_n}\end{bmatrix}_{\xi_i}\right)^{-1}\left(\sum_{i=0}^{N}\left[\Pi(t_i) - \widehat{\Pi}(t_i)_{\hat{\xi}_j}\right]\begin{bmatrix}\dfrac{\partial\widehat{\Pi}}{\partial\varsigma} \\ \dfrac{\partial\widehat{\Pi}}{\partial\omega_n}\end{bmatrix}_{\xi_i}\right) \tag{16}$$

In terms of the model parameters, Eq. (16) can be expressed as

$$\begin{bmatrix} \varsigma \\ \omega_n \end{bmatrix}_{j+1} = \begin{bmatrix} \varsigma \\ \omega_n \end{bmatrix}_{j} + \left(\begin{bmatrix} \sum_{i=0}^{N} \left(\frac{\partial \widehat{\Pi}}{\partial \varsigma} \right)^2 & \sum_{i=0}^{N} \left(\frac{\partial \widehat{\Pi}}{\partial \varsigma} \frac{\partial \widehat{\Pi}}{\partial \omega_n} \right) \\ \sum_{i=0}^{N} \left(\frac{\partial \widehat{\Pi}}{\partial \varsigma} \frac{\partial \widehat{\Pi}}{\partial \omega_n} \right) & \sum_{i=0}^{N} \left(\frac{\partial \widehat{\Pi}}{\partial \omega_n} \right)^2 \end{bmatrix}_{\xi_j} \right)^{-1} \left(\begin{bmatrix} \sum_{j=0}^{N} \left[\Pi(t_i) - \widehat{\Pi}(t_i)_{\xi_j} \right] \frac{\partial \widehat{\Pi}}{\partial \varsigma} \\ \sum_{j=0}^{N} \left[\Pi(t_i) - \widehat{\Pi}(t_i)_{\xi_j} \right] \frac{\partial \widehat{\Pi}}{\partial \omega_n} \end{bmatrix}_{\xi_i} \right) \tag{17}$$

In Eq. (17) N is the number of data points in the time history curve fit. The model derivatives necessary for calculating Eq. (17) are provided below for any damping ratio – overdamped (Eq. (18)), critically-damped (Eq. (19)), or underdamped (Eq. (20)).

$$\varsigma > 1$$

$$\Pi(t) = e^{-\varsigma \omega_n t} \left[\frac{\varsigma}{\sqrt{\varsigma^2 - 1}} \sinh\left(\sqrt{\varsigma^2 - 1}\ \omega_n t \right) + \cosh\left(\sqrt{\varsigma^2 - 1}\ \omega_n t \right) \right]$$

$$\frac{\partial \Pi(t)}{\partial \varsigma} = -\frac{e^{-\varsigma \cdot \omega_n t}}{\varsigma^2 - 1} \left[\frac{1}{\sqrt{\varsigma^2 - 1}} \cdot \sinh\left(\sqrt{\varsigma^2 - 1}\ \omega_n t \right) - \omega_n t \cdot \cosh\left(\sqrt{\varsigma^2 - 1}\ \omega_n t \right) \right]$$

$$\frac{\partial \Pi(t)}{\partial \omega_n} = -e^{-\varsigma \omega_n t} \left[\frac{t}{\sqrt{\varsigma^2 - 1}} \right] \cdot \sinh\left(\sqrt{\varsigma^2 - 1} \omega_n t \right) \tag{18}$$

$$\varsigma = 1$$

$$\Pi(t) = e^{-\omega_n t} (\omega_n t + 1)$$

$$\frac{\partial \Pi(t)}{\partial \varsigma} = \frac{1}{3} e^{-\omega_n t} (\omega_n t)^3$$

$$\frac{\partial \Pi(t)}{\partial \omega_n} = -\omega_n \cdot t^2 \cdot e^{-\omega_n t} \tag{19}$$

$$
\begin{aligned}
&\varsigma < 1 \\
&\Pi(t) = e^{-\varsigma\omega_n t}\left[\frac{\varsigma}{\sqrt{1-\varsigma^2}}\sin\left(\sqrt{1-\varsigma^2}\ \omega_n t\right) + \cos\left(\sqrt{1-\varsigma^2}\ \omega_n t\right)\right] \\
&\frac{\partial\Pi(t)}{\partial\varsigma} = \frac{e^{-\varsigma\cdot\omega_n t}}{1-\varsigma^2}\left[\frac{1}{\sqrt{1-\varsigma^2}}\cdot\sin\left(\sqrt{1-\varsigma^2}\ \omega_n t\right) - \omega_n t\cdot\cos\left(\sqrt{1-\varsigma^2}\ \omega_n t\right)\right] \\
&\frac{\partial\Pi(t)}{\partial\omega_n} = -e^{-\varsigma\omega_n t}\left[\frac{t}{\sqrt{1-\varsigma^2}}\right]\cdot\sin\left(\sqrt{1-\varsigma^2}\,\omega_n t\right)
\end{aligned}
\tag{20}
$$

3.3 Parameter Estimation and Best Fit Examples

The algorithm of the previous section was applied to three sets of data from previous tests described in Ref. [1], including the 8 pulse burn shown in Figure 6. The three sets of data used came from: 1) a vacuum chamber test of a high expansion ratio (9.5) nozzle; 2) a vacuum chamber test of a low expansion ratio (2.06) nozzle; and 3) an ambient environment test of the low expansion ratio (2.06) nozzle. Figure 1 and Table 1 describe the configuration of the rocket motor and nozzles used in these tests. Figure 12 compares the resulting data with the optimal second order model curve fits overlaid on the original data sets. For each fit, only the tail off portion of the time histories are used to estimate the corresponding second order parameters. Table 2 summarizes the resulting parameter estimates, along with the fit statistics and optimal model error estimates.

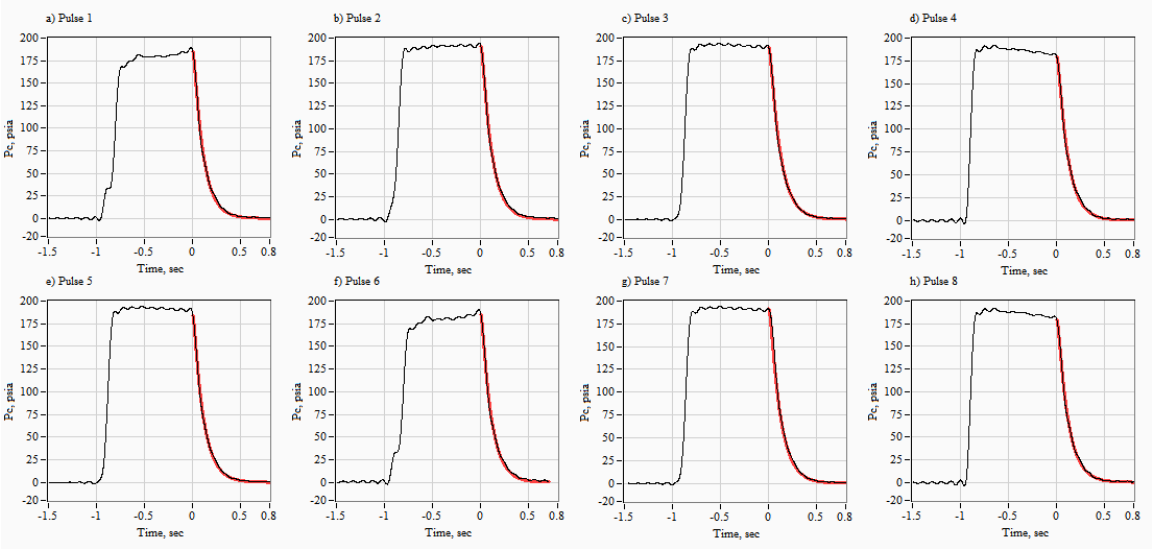

Fig. 12 Comparing Chamber Pressure Data to Second Order Tail-Off Curve Fits

Figure 12 shows the vacuum chamber test data with the high expansion ratio nozzle. The maximum likelihood parameter estimation was repeated for the low expansion ratio nozzle and ambient tests. The resulting second order model parameters for all three tests are shown in Table 2 below.

Table 2 Max Likelihood Estimates and Fit Statistics of 2nd Order Model Parameters

	High ER - Vacuum		*Low ER - Vacuum*		*Low ER - Ambient*	
Pulse No.	ζ	ω_n	ζ	ω_n	ζ	ω_n
1	1.652	29.093	1.119	27.578	0.813	28.371
2	1.543	26.025	1.095	26.830	0.741	23.400
3	1.523	24.376	1.142	27.744	0.703	22.341
4	1.549	25.581	1.121	27.088	0.725	22.323
5	1.814	31.253	1.364	33.469	0.728	23.200
6	1.657	28.945	1.323	31.927	0.742	23.862
7	1.524	24.380	1.166	34.013	0.730	22.975
8	1.576	25.850	1.100	32.224	-	-
Mean±95% Conf.	1.605± 0.083	26.938 ± 2.100	1.179 ± 0.087	30.109 ± 2.569	0.740± 0.032	23.782 ±1.938
St. Dev.	0.100	2.514	0.105	3.075	0.035	2.098

The mean data presented in Table 2 also shows the uncertainty range based on the student-t distribution with 95% confidence level for the appropriate number of degrees of freedom for that particular column of values. The student-t confidence interval is calculated as[19]

$$\bar{x} - \tau_{c\%} \cdot \frac{\bar{S}_x}{\sqrt{n}} \leq \mu \leq \bar{x} + \tau_{c\%} \cdot \frac{\bar{S}_x}{\sqrt{n}} \tag{21}$$

where $\{x,S_x\}$ are the sample mean and standard deviation, n us the number of tests, μ is the true mean, and $\tau_{c\%}$ is the t-multiplier for *c%* confidence level and *n-1* degrees of freedom. Based on these second order model curve fits, the time constants, τ, is calculated for each pulse, and averaged for each test by $\tau = 2\varsigma/\omega_n$, and the results are tabulated in Table 3. Clearly the high expansion ratio nozzle in the vacuum chamber has the largest time constant, and the most lag in pressure sensing. Of the two low expansion ratio data sets, the vacuum chamber test has the larger time constant, with the ambient test having the smallest of all three.

Table 3 Time Constants Based on Second Order Model

	High ER - Vacuum	*Low ER - Vacuum*	*Low ER - Ambient*
Pulse No.	τ (s)	τ (s)	τ (s)
1	0.114	0.081	0.057
2	0.119	0.082	0.063
3	0.125	0.082	0.063
4	0.121	0.083	0.065
5	0.116	0.082	0.063
6	0.114	0.083	0.062
7	0.125	0.069	0.064
8	0.122	0.068	-
Mean±95% Conf.	0.119 ± 0.004	0.079 ± 0.005	0.062 ± 0.002
St. Dev.	0.004	0.006	0.002

This result, with the ambient test conditions showing the lowest associated response latency, is consistent with physical observations. During the ambient testing campaign the plume exhausted to open air, thereby giving the exhaust by-products room to partially dissipate. However, as shown by Figure 6d, during the vacuum tests the vacuum pump could not entirely keep up with the exhaust gasses generated by the thruster and sooty plume by-products tended to accumulate within the vacuum chamber and deposited on all surfaces, including the internal motor geometry. This internal accumulation was likely a result of backflow that occurred during the motor startup and tail-off transients.

CHAPTER 4

USING OPTIMAL DECONVOLUTION TO RECONSTRUCT THE CHAMBER PRESSURE SIGNALS

Once the tail off data are used to calculate the damping ratio and natural frequencies, the second order model can then be used to reconstruct the attenuated pressure signals. This method uses the optimal-deconvolution algorithm developed by Ref. [3]. The method assumes that the model parameters remain constant over the burn duration. The deconvolution algorithm belongs to a class of optimization problems that was first solved by Norbert Wiener in the frequency domain, and later extended to the time-domain by Rudolf Kálmán.[20,21] The model inversion equation, as developed by Wiener, is presented in Eq. (23).

$$\hat{P}_c(\omega) = \left\{ \frac{\Upsilon(\omega)^* \left(\frac{\left|\left|P_{00}\right|\right|^2}{\left|\left|N\right|\right|^2} \right)_\omega}{\left|\left|\Upsilon(\omega)\right|\right|^2 \left(\frac{\left|\left|P_{00}\right|\right|^2}{\left|\left|N\right|\right|^2} \right)_\omega + 1} \right\} P_L(\omega) \tag{23}$$

In Eq. (23) the transfer function, represented by the Fourier transform of Eq. (5), is

$$\frac{P_L(\omega)}{P_c(\omega)} = \Upsilon(\omega) = \frac{\omega_n^2}{(j\omega)^2 + 2\cdot\varsigma\cdot\omega_n\cdot j\omega + \omega_n^2} = \frac{1}{1 - \left(\frac{\omega}{\omega_n}\right)^2 + 2j\cdot\varsigma\cdot\left(\frac{\omega}{\omega_n}\right)} \tag{24}$$

The deconvolution algorithm amplifies attenuated pressure signals, while selectively rejecting sensor noise. The filter noise scaling parameter, $\left(\left|\left|P_{00}\right|\right|^2 / \left|\left|N\right|\right|^2 \right)_w$, although technically representing the mean-square signal-to-noise ratio of the unknown input signal, can be approximated by the square of the signal-to-noise ratio (S/N) of the

measured output signal. This ratio may be constant (white-noise) or vary as a function of measurement input frequency (colored-noise). The Wiener solution weighs the Fourier coefficients to compensate for the S/N of the system as a function of the input signal frequency. Adaptive Wiener filtering algorithms that estimate the S/N as a part of the filtering process have been developed,[22] but will not be applied here. The S/N values are selected a priori based on the observed noise threshold of the measured pressure signal.

The model of Eq. (24) is implemented using spectral methods. The Discrete Fourier Transform[23] (DFT) of the input is multiplied by the Wiener transfer function calculated using Eqs. (23), and (24) for each of the corresponding spectral frequencies of the DF. The resulting spectrum is then inverse-transformed to calculate the Wiener-optimal output time history. To ensure that the reconstructed time series is real-valued, it is necessary to build the "upper half" of the spectrum before performing the inverse transform. Building the upper portion of the spectrum involves folding the complex conjugate of the spectrum below the Nyquist frequency[24] about the Nyquist frequency. The upper half of the spectrum is concatenated with the lower half of the spectrum, and the resulting frequency spectrum is transformed to the time domain via the inverse DFT.

4.1 Example Reconstructed Chamber Pressure Time Histories

Using the mean values for ζ and ω_n from Table 2, the deconvolution algorithm of Eq. (23) was applied to the attenuated chamber pressure pulses presented in Figures 6, 7, and 12, and to the low expansion ratio tests. Figure 13 presents an example calculation – the first four pulses from the high expansion ratio nozzle vacuum chamber test. Plots (a) through (d) compare the original pulse time histories against the reconstructed data. Figure 13 (e) through (h) also re-plot the oxidizer massflow data from Figure 6 and 7 for

reference. For all pressure pulses, the reconstructed chamber pressure data exhibit a time lead shift of approximately 50 ms, with a considerable sharpening of the tail off pressure. Note that the initial ignition transient, completely attenuated by the chamber pressure sensor configuration, is highly amplified and agrees reasonably with the transients observed on the oxidizer massflow plots. Figure 14 shows a detailed look at the deconvolved and original chamber pressure signals overlaid on the oxidizer massflow time history for the first two pulses as examples. It can clearly be seen that the reconstructed chamber pressure signal closely follows the oxidizer massflow tail-off, providing reassurance that the sensor lag has been predicted and removed accurately.

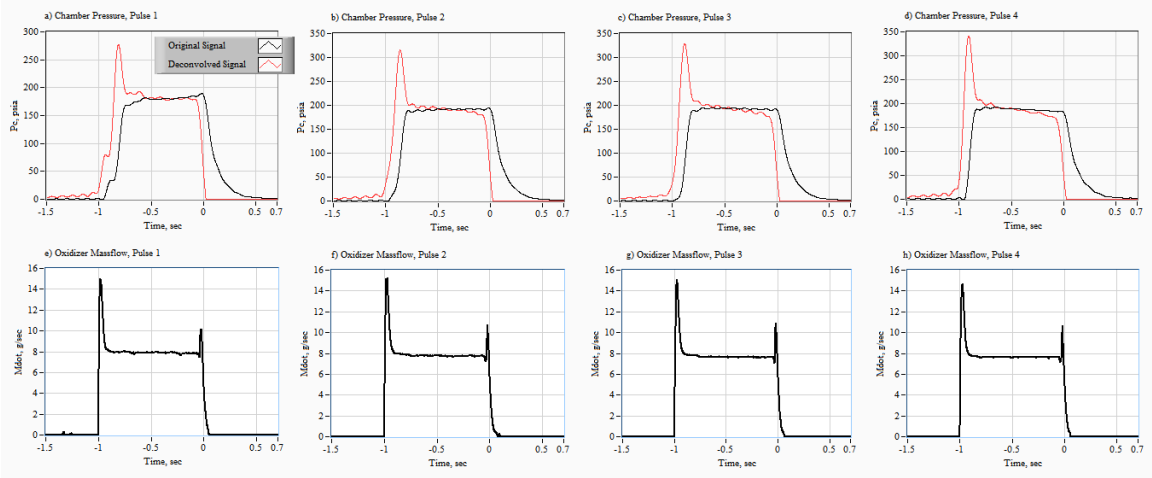

Fig. 13 Reconstructed Chamber Pressure Pulses Compared with Oxidizer Massflow

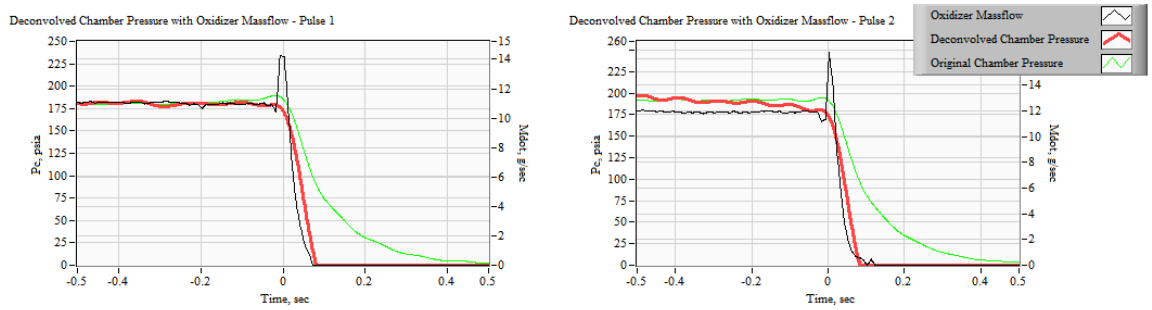

Fig. 14 Reconstructed vs. Original Pressure Signal Overlaid on Massflow Tail Off

CHAPTER 5

RESULTS AND DISCUSSION

Although the inline GOX venturi measures the oxidizer mass flow in real-time, the test stand could not measure real time fuel mass flow. Thus, for this testing campaign reference [1], calculated the "instantaneous" fuel mass flow rates as the difference between the measured nozzle exit and oxidizer mass flow rates,

$$\dot{m}_{fuel} = \dot{m}_{total} - \dot{m}_{ox} \tag{25}$$

The nozzle exit mass flow time history was calculated from the measured chamber pressure P_0 time history, the nozzle throat area, A^*, and the exhaust gas properties (ratio of specific heat, γ, and specific gas constant, R_g) using the 1-dimensional choking mass flow equation,

$$\dot{m}_{total} = A^* \cdot P_0 \cdot \sqrt{\frac{\gamma}{R_g \cdot T_0} \cdot \left(\frac{2}{\gamma+1}\right)^{\frac{\gamma+1}{\gamma-1}}} \tag{26}$$

The total amount of fuel consumed during the bun is calculated by

$$\Delta M_{fuel} = \int_0^t \left(\dot{m}_{total} - \dot{m}_{ox}\right) \cdot dt \tag{27}$$

The instantaneous oxidizer O/F ratio is estimated by

$$O/F = \frac{\dot{m}_{ox}}{\dot{m}_{total} - \dot{m}_{ox}} \tag{28}$$

For each data point in the burn time history, two-dimensional tables of thermodynamic and transport properties were interpolated to calculate the gas constant R_g, ratio of specific heats γ, and flame temperature T_0. The table of equilibrium properties of the GOX/ABS exhaust plume were developed by Ref. [7] using the with measured

chamber pressure P_0, combustion efficiency η*, and mean O/F ratio as independent look up variables for the tables. The lookup tables were generated using the NASA's industry standard Chemical Equilibrium Analysis code (CEA)[25] to perform the chemistry calculations.

Each fuel grain was burned multiple times to allow interim fuel mass consumption measurements between burns. The corresponding oxidizer mass consumed was calculated by integrating the venturi mass flow time history over the burn duration. The mean O/F ratio over the burn duration was estimated by dividing the consumed oxidizer mass by the consumed fuel mass. By adjusting η*, the flame temperature was scaled by

$$T_{0_{actual}} = \eta^{*2} \cdot T_{0_{ideal}} \tag{29}$$

The adjusted the nozzle-exit massflow and the resulting consumed fuel massflow. Adjusting input combustion efficiency upwards has the effect of increasing the calculated fuel mass consumption, and downwards decreases the calculated fuel mass consumption. The fuel massflow calculation starts with an assumed combustion efficiency of η^* = 0.90. The calculations of Equations (25)-(29) were iterated, adjusting η^* until the calculated fuel mass equals the measured fuel mass to within 0.5% accuracy.

Unfortunately, the chamber pressure attenuation and phasing mismatch with the oxidizer massflow measurements was a major source of inaccuracy. Using the prescribed methods, the amplified fidelity chamber pressure reconstruction provides the ability to re-calculate the fuel massflow burn rates and regression rates much more accurately, and with objective precision. These values can then be used to determine more accurately the specific impulse, I_{sp}, characteristic velocity, C^*, and O/F ratio. Table 4, 5, and 6

summarize the original and modified values based on the updated massflow rates from the deconvolved chamber pressure signals for the high expansion ratio vacuum, low expansion ratio vacuum, and low expansion ratio ambient tests, respectively.

Table 4 Pre- and Post-Deconvolution Motor Parameters, High ER Nozzle - Vacuum

Pulse No.	*Original* I_{sp}	*Mod.* I_{sp}	*Original* C^*	*Mod.* C^*	*Mod.O/F Ratio*
1	265.563	271.397	1577.480	1612.130	2.808
2	257.602	273.964	1574.180	1674.170	2.176
3	262.363	285.447	1577.810	1716.640	2.105
4	271.353	293.927	1581.850	1713.440	2.022
5	260.802	279.999	1578.710	1694.910	2.048
6	264.325	271.207	1580.960	1622.120	2.811
7	258.213	279.023	1575.220	1702.180	2.089
8	255.365	276.883	1564.980	1696.850	2.018
Mean±95% Conf. Inter.	261.948 ± 4.293	278.981 ± 6.423	1576.399 ± 4.417	1679.055 ± 33.775	2.260 ± 0.287
St. Dev.	5.139	7.688	5.288	40.430	0.343

Table 5 Pre- and Post-Deconvolution Motor Parameters, Low ER Nozzle - Vacuum

Pulse No.	*Original* I_{sp}	*Mod.* I_{sp}	*Original* C^*	*Mod.* C^*	*Mod.O/F Ratio*
1	225.947	225.145	1486.570	1487.400	3.296
2	225.019	249.467	1453.310	1595.580	2.653
3	235.086	241.176	1518.420	1557.760	3.339
4	235.162	251.174	1515.260	1618.430	2.665
5	236.318	239.754	1591.240	1614.370	2.745
6	235.432	245.340	1587.120	1653.910	2.393
7	222.508	231.838	1461.220	1522.490	3.013
8	223.347	240.761	1451.390	1564.560	3.082
Mean±95% Conf. Inter.	229.852 ± 5.124	240.582 ± 7.266	1508.066 ± 47.039	1576.813 ± 45.645	2.898 ± 0.281
St. Dev.	6.134	8.698	56.307	54.638	0.800

Table 6 Pre- and Post-Deconvolution Motor Parameters, Low ER Nozzle - Ambient

Pulse No.	*Original* I_{sp}	*Mod.* I_{sp}	*Original* C^*	*Mod.* C^*	*Mod.O/F Ratio*
1	207.615	213.565	1528.490	1572.300	3.292
2	209.168	214.749	1522.940	1563.570	3.133
3	209.899	215.780	1523.840	1566.530	3.137
4	206.901	211.603	1523.910	1558.540	3.056
5	211.036	216.282	1529.770	1567.790	3.182
6	209.565	213.910	1529.950	1561.670	3.118
7	212.607	217.462	1531.510	1566.480	3.166
Mean±95% Conf. Inter.	209.542 ± 1.793	214.764 ± 1.800	1527.201 ± 3.260	1565.269 ± 4.132	3.155 ± 0.067
St. Dev.	1.940	1.948	3.528	4.472	0.073

5.1 Comparison to Analytical Predictions

By averaging the achieved chamber and ambient or vacuum pressures over the burn duration, the nozzle geometries of Table 1, and the flow properties calculated from the analysis of Eqs. (25) - (29), theoretical values for C_F, C^*, and I_{sp} were calculated using the one-dimensional isentropic de-Laval flow equations[26], where

$$C_F = \frac{F}{P_0 \cdot A^*}, \quad C^* = \frac{P_0 \cdot A^*}{\dot{m}}, \text{ and } I_{sp} = \frac{C_F \cdot C^*}{g_0}. \tag{30}$$

Figure 15 summarizes these results. Plotted are the specific impulse values for a) 9.5:1 ER nozzle under vacuum conditions (~ 12 kPa), b) 2.06:1 ER nozzle under vacuum conditions (~ 12 kPa), and c) 2.06:1 ER nozzle under ambient test conditions (~ 86, kPa). On each sub-plot four specific impulse points are plotted, a) the original I_{sp} calculated using the attenuated chamber pressure data, b) the modified I_{sp} calculated using the re-constructed chamber pressure data, and c) the theoretical I_{sp} for the nozzle expansion ratio and the vacuum/ambient test conditions, and d) the theoretical I_{sp} value that would

be achieved for the optimal expansion ratio, and at the test conditions. The student-t uncertainty bounds from Tables 4-6 and also plotted.

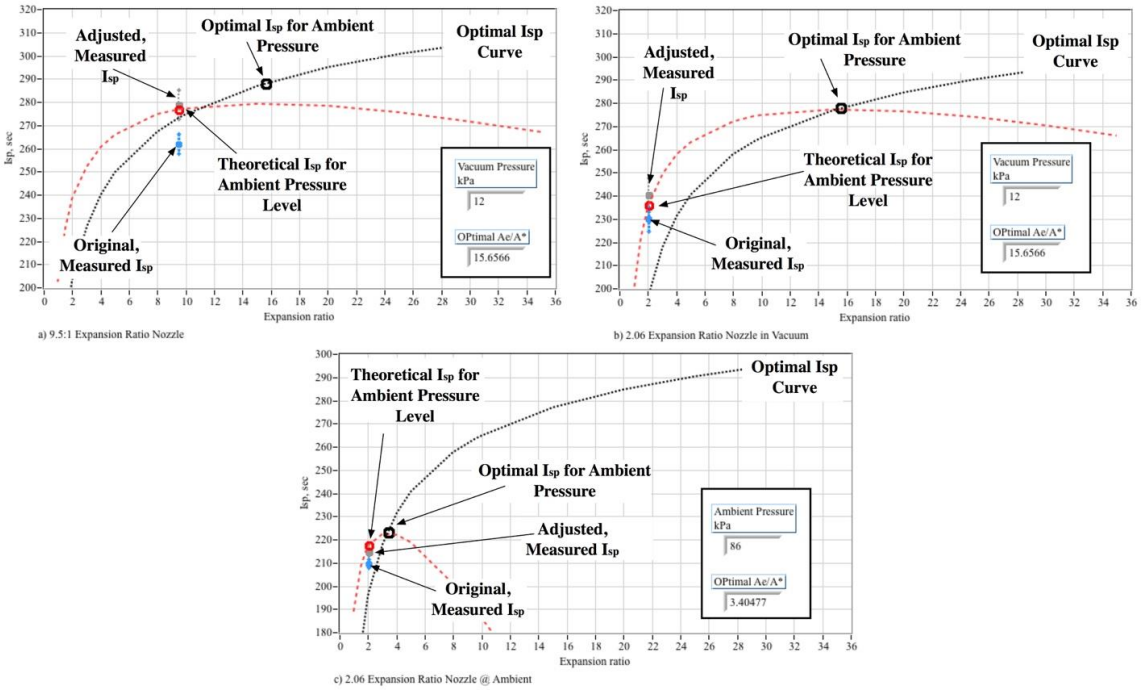

Fig. 15 Theoretical and Measured Specific Impulse Comparisons

Inspecting Figure 15(a) for the 9.5:1 ER nozzle, tested under vacuum conditions, the predicted I_{sp} is approximately 276.73 sec. This value compares with 261.95 sec for the original highly-attenuated data, and 278.98 sec for the modified value calculated using the reconstructed chamber pressure data. Thus, the agreement between the adjusted I_{sp} data is within 95% student-t the uncertainty levels shown by Table column 3. These agreements with theory help validate that the deconvolution improves the accuracy of the chamber pressure signal.

Inspecting Figure 15(b) for the 2.06:1 ER nozzle, tested under vacuum conditions, it becomes obvious that the low expansion ratio nozzle is significantly under-expanded, and the theoretical prediction "splits" the difference between the original and adjusted

specific impulse values. Because the uncertainty levels for the original and adjusted data overlap, it must be concluded that the differences between original and modified specific impulse values are statistically insignificant.

Finally, inspecting Figure 15(c) for 2.06:1 ER nozzle, tested under ambient conditions, shows a theoretical I_{sp} of 217.69 sec compared to 209.54 sec for the original data and 214.76 for the modified data. Although the pressure adjustment does produce a statistically significant better agreement with the theoretical prediction, the change between the original and modified values is significantly lower than occurs with the vacuum tests. This observation agrees with the previously-discussed notion that the exhaust products cause more contamination of the pressure sensing lines in the vacuum chamber than in an ambient environment, where the exhaust can spread out and away from the system. In other words, the deconvolution has less of an impact when contamination is less of an issue. Even with these comparatively smaller changes, the deconvolved results match up closer with isentropic nozzle theory than the original values.

Finally, on Figures 15(a) and(b), note that for the vacuum test conditions and the mean operating mean chamber pressure level, the optimal expansion ratio for the operating vacuum chamber pressure level is predicted to be 15.67. At this ER the calculated "optimal" I_{sp} is 288.03 sec. Thus, the 9.5:1 nozzle was actually slightly under expanded for the operating vacuum conditions. The images of Figure 16 show that both the low expansion ratio (2.06:1), and higher expansion ratio (9.5:1) nozzles were under expanded for the vacuum test conditions. Note in Figure 16 (a) that the plume from the 2.06:1 nozzle expands rapidly for the 5^{o} exit angle to slightly less than 25^{o} before the

pressure equalizes and the flow angle begins to flatten out. In contrast the 9.5:1 nozzle plume spreads less but still significantly after leaving the nozzle exit.

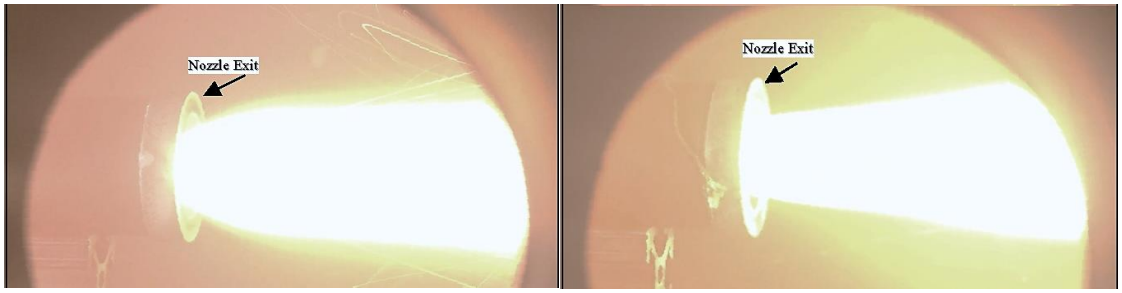

a) 2.06:1 ER Nozzle Exhaust Plume b) 9.5:1 ER Nozzle Exhaust Plume

Fig. 16 Exhaust Plumes in Vacuum Chamber for Low and High ER Nozzles

Based on the observed good-agreement between the predicted and adjusted data I_{sp} values, one can extrapolate the optimal thruster performance to hard vacuum conditions by following the optimal I_{sp} curve -- the dashed black line -- of 15 (a) to higher expansion ratios. Based on this projection it is concluded that the thruster will reach a vacuum I_{sp} level greater than 300 seconds when the nozzle expansion ratio grows to 24:1.

CHAPTER 6

SUMMARY AND CONCLUSION

The Propulsion Research Laboratory at Utah State University has recently developed a promising "green" alternative to current space propulsion systems that are based on environmentally unsustainable, highly toxic propellants like hydrazine and nitrogen tetroxide. After initial proof of concept tests were completed, an effort was made to scale down the thruster to a flight-weight system that would be generally applicable for SmallSat operations. The resulting 25-N flight weight system was ground tested under both ambient pressure and vacuum conditions. The 25-N motor tended to produce a behavior that became increasingly fuel-rich during the burn lifetime. Fuel-rich operation of the thrust chambers eventually introduces contaminants into the pneumatic arrangement used to deliver the chamber pressure to the sensing pressure transducer. When the transmission tubes were partially-clogged with burned hydrocarbons, a significant drop in the measurement response fidelity occurred. This attenuation significantly compromised the test results.

Contamination effects were especially strong during the vacuum burns. Cleaning the hydrocarbons from the tubing is extremely difficult, and often requires that the sensors be disassembled and the transmission tubing must be completely replaced. Reassembling the systems and repeating the tests, continually cleaning the chamber pressure assembly between tests, was both economically and practically infeasible. Instead an analytical method was developed whereby maximum-likelihood techniques were used to optimally fit a second order model to chamber pressure response, and the resulting model was subsequently used to reconstruct a high-fidelity motor response

using optimal deconvolution. Based on the observed good-agreement between the predicted and adjusted data specific impulse values, it is concluded that the thruster will reach a vacuum I_{sp} level greater than 300 seconds when the nozzle expansion ratio grows to 24:1.

The presented method offers a useful tool for obtaining unsteady pressure measurements and represents an alternative to conventional in-situ mounting methods for measuring high frequency fluctuating pressures in difficult or hostile environments. When properly tuned, the derived-method amplifies the attenuated pressure signals while selectively rejecting the contaminating measurement noise. The model offers the potential to return fidelity to measurements that are otherwise highly attenuated.

Because of the unpredictable effects of the combustion product contamination within the pressure transmission lines, fittings, and other components, a purely analytical method could not be used for this analysis. Instead, the natural response decay of the chamber pressure trace, after the termination of oxidizer flow for each thruster pulse is curve fit with a second-order response model, and this transfer function is used to perform the optimal deconvolution of the highly attenuated pressure signal.

The test data and computations derived from the previous ambient and vacuum testing campaigns were re-examined using the reconstructed chamber pressure data in place of the original highly-attenuated measurements. The updated chamber pressure traces led to calculations of specific impulse and characteristic velocity that are more consistent with isentropic nozzle theory compared to the original data. It is clear from the time constants of the pressure tail-off curve fits that vacuum chamber tests, where combustion products are more contained, cause larger lag in pressure sensing compared

to ambient environment tests. Furthermore, where O/F ratios are lower (more fuel-rich), and combustion exhaust products are more concentrated, more severe attenuation in chamber pressure signals is observed. The latency in the pressure sensor signals has been shown to be tied to the level of concentration and confinement of combustion products. When this lag is corrected using optimal deconvolution based on second order models fit to the pressure tail-offs, the motor parameters more closely match those predicted by theory.

REFERENCES

[1] Whitmore, S. A., and Bulcher, A. M., "Vacuum Test of a Novel Green-Propellant Thruster for Small Spacecraft", AIAA 2017-5044. *53rd AIAA/SAE/ASEE Joint Propulsion Conference*, AIAA Propulsion and Energy Forum, https://doi.org/10.2514/6.2017-5044

[2] Zilliac, G., and Karabeyoglu, M., A., "Hybrid Rocket Fuel Regression Rate Data and Modeling," AIAA Paper 2006-4504, July 2006. https://doi.org/10.2514/6.2006-4504

[3] Whitmore, S., A., and Wilson, M. D., "Wiener Deconvolution for Reconstruction of Pneumatically Attenuated Pressure Signals", *AIAA Journal*, Vol. 49, No. 5 (2011), pp. 890-897. https://doi.org/10.2514/1.J050102

[4] Berg, H., and Tijdeman, H., "Theoretical and Experimental Results for the Dynamic Response of Pressure Measuring Systems," National Aerospace Lab., NLR-TR F.238, Amsterdam, Jan. 1965. https://dor.org/ 10.13140/2.1.4790.1123

[5] Whitmore, S. A., and Fox, B., "Improved Accuracy, Second-Order Response Model for Pressure Sensing Systems", *Journal of Aircraft*, Vol. 46, No. 2 (2009), pp. 491-500. https://doi.org/10.2514/1.36262

[6] Maine, R. E., and Iliff, K. W., "Application of parameter estimation to aircraft stability and control: The Output Error Approach," *NASA RP 1168*, Edwards CA, 1968. https://www.nasa.gov/centers/dryden/pdf/88044main_H-1299.pdf

[7] Whitmore, S. A., Peterson, Z. W., and Eilers, S. D., “Comparing Hydroxyl Terminated Polybutadiene and Acrylonitrile Butadiene Styrene as Hybrid Rocket Fuels,” *J. Propulsion and Power*, Vol. 29, No. 3, May-June 2013. Pp. 582-592. https://dio.org/10.2514/1.B34924

[8] Whitmore, Stephen A., Nathan R. Inkley, Daniel P. Merkley, and Michael I. Judson. "Development of a Power-Efficient, Restart-Capable Arc Ignitor for Hybrid Rockets", *Journal of Propulsion and Power*, Vol. 31, No. 6 (2015), pp. 1739-1749. DIO: https://dio.org/10.2514/1.B35595

[9] Whitmore, Stephen A., Merkley, Stephen L., Zachary S., Walker, Sean D., “Development of a Power Efficient, Restartable, "Green" Propellant Thruster for Small Spacecraft and Satellites,” SSC15-P-34, 29th *AIAA/USU Conference on Small Satellites*, Logan UT, 8-13 August, 2015. https://digitalcommons.usu.edu/smallsat/2015/all2015/90/

[10] Whitmore, S. A., and Merkley, S. L., "Effects of Radiation Heating on Additively Printed Hybrid Fuel Grain O/F Shift", AIAA 2016-4867, 52nd *AIAA/SAE/ASEE Joint Propulsion Conference, Propulsion and Energy Forum*, Salt Lake City, UT, 28-30 July, 2016. https://doi.org/10.2514/6.2016-4867

[11] Whitmore, S. A., and Mathias, S., "Development and Testing of Three Alternative Designs for Additively Manufactured Hybrid Thrusters", AIAA 2016-4867, 52nd *AIAA/SAE/ASEE Joint Propulsion Conference, Propulsion and Energy Forum*, Salt Lake City, UT, USA, July 25-18, 2016. https://doi.org/10.2514/6.2016-5068

[12] Whitmore, S. A., and Brewer, D. L., "Plume Contamination Measurements of an Additively-Printed GOX/ABS Hybrid Thruster", AIAA 2017-4982, 53rd AIAA/SAE/ASEE Joint Propulsion Conference, *AIAA Propulsion and Energy Forum*, July, 2017, https://doi.org/10.2514/6.2017-4982

[13] Whitmore, Stephen A., "Additively Manufactured Acrylonitrile-Butadiene-Styrene–Nitrous-Oxide Hybrid Rocket Motor with Electrostatic Igniter", *J. Propulsion and Power*, Vol. 31, No. 4 (2015), pp. 1217-1220. https://doi.org/ 10.2514/1.B35681

[14] Whitmore, Stephen A., "Additive Manufacturing as an Enabling Technology for "Green" Hybrid Spacecraft Propulsion," RAST-1039, *Conference on Recent Advances in Space Technology 2015*, Istanbul Turkey, June 16-19 2015. https://ieeexplore.ieee.org/document/7208305

[15] Whitmore, S. A., and Stephen L. Merkley, S. L., "Effects of Radiation Heating on Additively Printed Hybrid Fuel Grain O/F Shift", AIAA 2016-4867, 52nd AIAA/SAE/ASEE Joint Propulsion Conference, *AIAA Propulsion and Energy Forum*, (AIAA 2016-4867) Salt Lake City UT USA, July 2016. https://doi.org/10.2514/6.2016-4867

[16] Gordon, S., and McBride, B. J., "Computer Program for Calculation of Complex Chemical Equilibrium Compositions and Applications," *NASA RP-1311*, 1994. https://www.grc.nasa.gov/www/CEAWeb/RP-1311.pdf

[17] Whitmore, S. A., "MAE 5540 Propulsion Systems, Section 6: Modeling Transient Rocket Operation," slides 15-16, http://mae-nas.eng.usu.edu/MAE_5540_Web/propulsion_systems/section6/section.6.1.pdf, [Retrieved 24 January, 2018]

[18] Taylor, Lawrence W., Jr.; and Iliff, Kenneth W. "Systems Identification Using a Modified Newton-Raphson Method: A FORTRAN Program", NASA TN D-6734, 1972. https://ntrs.nasa.gov/archive/nasa/casi.ntrs.nasa.gov/19720014931.pdf

[19] Hogg, R. V.; Craig, A. T., *Introduction to Mathematical Statistics, 7th ed.*, Macmillan & Sons, Inc., New York, 1978, ISBN-13: 978-0321795434, ISBN-10: 0321795431, pp. 141-206.

[20] Meditch, J. S., *Stochastic Optimal Linear Estimation and Control*, McGraw-Hill, 1969, pp. 288-322. https://ieeexplore.ieee.org/document/4309146

[21] Kalman, R. E., "New Methods in Wiener Filtering Theory," *Proceedings of the First Symposium on Engineering Applications of Random Function Theory and Probability*, John Wiley & Sons, Inc., New York, 1963, pp. 270-388. https://scinapse.io/papers/184894097

[22] Gonzalez, R., Woods, R., and Eddins, *S. Digital Image Processing Using Matlab*, Prentice Hall, Saddle River, NJ, 2003, Chapt. 4. https://www.mathworks.com/discovery/digital-image-processing.html

[23] Otnes, R., K., and Enochson, L., *Applied Time Series Analysis*, John Wiley and Sons, New York, 1978, pp. 219-260. https://doi.org/10.1121/1.383336

[24] Beckwith, T. G., Marangoni, R. D., and Lienhard V, J. H., *Mechanical Measurements, 6th Ed.*, Prentice Hall, 2006, pp.85-145. ISBN-13: 9780201847659

[25] Gordon, S., and McBride, B. J., "Computer Program for Calculation of Complex Chemical Equilibrium Compositions and Applications," *NASA RP-1311*, 1994.

[26] Anderson, J. D. Jr., Modern Compressible Flow with Historical Perspective, 3rd ed., McGraw-Hill, New York, 2003, pp. 127-187.